Relaxation dynamics in the self-propelled Voronoi model for epithelial monolayers

Meng-Yuan Li and Yan-Wei Li*

Key Laboratory of Advanced Optoelectronic Quantum Architecture and Measurement (MOE), School of Physics, Beijing Institute of Technology, Beijing 100081, China

(Received 24 January 2024; accepted 2 August 2024; published 23 August 2024)

Cell monolayers and epithelial tissues display slow relaxation dynamics during the reversible transition between mesenchymal and epithelial cells, a phenomenon directly relevant to embryogenesis, tumor metastases, and wound healing. In active cells, persistent motion induces collective dynamics that significantly influence relaxation behavior. To better understand the role of persistence in cell relaxations, we perform extensive simulations and employ cage-relative measures to address the previously overlooked system size effects in model active cells. We identify the glass transition at various persistence values, demonstrating conventional near-equilibrium supercooled dynamics at low persistence. However, highly persistent cells exhibit distinctive intermittent dynamics associated with intermittent local T1 transitions, where cell velocity correlates over space with a characteristic length ξ. More significantly, we formulate a universal relationship predicting the global relaxation time based on the T1 transition and the spatial velocity correlation across a wide range of persistence values. Specifically, the relaxation time demonstrates a power-law dependence on the irreversible T1 transition rate, multiplied by $\exp(\xi)$. Here, ξ vanishes at small persistence in nearly equilibrated cells, and the irreversible T1 transition rate diminishes towards the mode-coupling glass transition point.

DOI: 10.1103/PhysRevResearch.6.033209

I. INTRODUCTION

Active systems harness energy from the environment, drive themselves significantly beyond equilibrium, and induce persistent motion among their constituents [1,2]. Among these, active cells have been intensely explored [3–10]. It has been found that, depending on cell deformability and mobility, active cells in biological tissues exhibit a reversible transition from fluidlike mesenchymal cells to a solidlike epithelial layer [3–5]. These transitions play crucial roles in various biological processes, such as organ development, tumor metastases, and wound healing [7,11–18].

Recent experiments and simulations have revealed that tissue fluidization has many similarities to the glass transition in both passive and active conditions [3,19–23]. For instance, typical supercooled dynamics occur during this transition. They include the caging behavior where cells are confined by their neighbors, a two-step relaxation process involving initial rattling of cells within the cage (β relaxation) succeeded by long-range motion following cage escape (α relaxation), and collective and heterogeneous dynamics [3,19,20,22,23]. In addition to the typical slow and heterogeneous dynamics, active systems may exhibit a variety of intriguing phenomena, such as emergent collective motion and intermittent dynamics. Collective behavior belongs to the category of dynamic self-assembly, characterized by spatial correlations and non-Gaussian distributions of velocity or displacement. This phenomenon has been widely observed in various systems, including active particles [24–27], fish schools [28], and bacterial colonies [29]. Intermittent dynamics, characterized by sequences of jumps between mechanical equilibria, arise from the balance between self-propulsion forces and interacting forces [27,30,31]. Previous studies identified the collective behavior as well as the intermittency of both global kinetic energy and local plastic events at large persistence in active particulate systems with pair interactions in two dimensions [27,30]. However, such intermittency is absent in three dimensions due to the inability to achieve force balance conditions [32].

Unlike particulate systems with simple pair interactions, soft polymeric particles—such as biological tissues [3,5,33], star polymers [34–36], dendrimers [37], microgels [38], polyelectrolyte stars [34], and soft granular particles [39,40]—deform when stressed by their neighbors, indicating that their interparticle interactions are of a many-body type. Additionally, plastic rearrangements primarily depend on topological T1 processes, which are the main mechanism for cell neighbor exchanges [23,33,41,42]. In active cells, intermittent T1 transitions are observed when neighbor exchanges are artificially controlled [6]. This intermittent phenomenon may not be attributed to the force balance mechanism mentioned above. It remains uncertain whether and under what conditions intermittent dynamics occur in freely evolving self-propelled cells. The intrinsic relationship between local topological T1 processes, collective motion, and global long-time α relaxation remains elusive. Furthermore,

*Contact author: yanweili@bit.edu.cn

most previous studies on two-dimensional (2D) cells focused on relatively small systems comprising several hundred cells. The contribution of system size effects to the dynamics of 2D active cells remains a topic of debate. In contrast to 2D thermal systems, where long-wavelength fluctuations lead to a strong dependence on system size [43–46], such fluctuations may be suppressed in active systems [47].

In this work, we explore the interplay between deformability and mobility in active cells and investigate the resulting relaxation dynamics. Our analysis reveals hitherto unexplored system size effects stemming from long-wavelength fluctuations in cells with small persistence, effectively addressed through cage-relative (CR) measures. Conversely, extended systems are required to account for additional nonequilibrium effects at large persistence. After mitigating these size effects, we identify the glass transition line in the plane of persistence time and deformability. We identify intermittent kinetic energy and the associated intermittent T1 transitions at large persistence, shaping a distinctive relaxation process. The distinct relaxation modes at short and long persistence times are encapsulated in a universal function describing the close correlation of the α relaxation time with the irreversible T1 transition rate and the length scale of spatial velocity correlations.

II. MODEL AND METHODS

We study the polydisperse self-propelled Voronoi model describing an active system of confluent epithelial cells [3,33,48–52]. The configurational degrees of freedom are the centers of mass of the cells $\{\mathbf{r}_i\}$, and their Voronoi tessellations determine the shapes of the cells. The mechanical energy of a cell depends on its area A_i and perimeter P_i, $E_i = K_A(A_i - A_0^i)^2 + K_P(P_i - P_0^i)^2$, where A_0^i and P_0^i are preferred values, while K_A and K_P are area and perimeter elastic constants. The two quadratic terms are from biological considerations [3,21,33,48–51,53]. Hence, the dimensionless energy functional is

$$e = \sum_{i=1}^{N} \left[\left(a_i - a_0^i\right)^2 + r^{-1}\left(p_i - p_0^i\right)^2 \right], \tag{1}$$

where $a_i = A_i/l^2$ and $p_i = P_i/l$, with l being the unit of length which we have chosen so that $\langle a_i \rangle = 1$. We fix the inverse perimeter modulus, $r = K_A l^2/K_P$, and the mass of cells m to unity. The preferred area a_0^i is uniformly distributed in the range 0.8–1.2 to avoid crystallization, while the preferred perimeter is fixed to $p_0^i = p_0\sqrt{a_0^i}$, with p_0 being the target shape index, which biologically characterizes the competition between cell-cell adhesion and cortical tension and determines the cell deformability [49,54]. Higher values of p_0 correspond to more deformable cells.

Cell centers $\{\mathbf{r}_i\}$ evolve according to the overdamped equations of motion $\zeta \frac{d\mathbf{r}_i}{dt} = \mathbf{f}_i^m + \mathbf{f}_i^a$ [3], where $\mathbf{f}_i^m = -\nabla_i e$ is the mechanical interaction force. ζ is the frictional coefficient, which also sets our time unit $\tau = \zeta/(K_A l^2)$. $\mathbf{f}_i^a = v_0 \hat{n}_i$ is the self-propulsion force with constant magnitude $v_0 = 1$ and is directed along the polarity vector $\hat{n}_i = (\cos\theta_i, \sin\theta_i)$, where the polarity angle θ_i is perturbed by $\partial_t \theta_i = \eta_i$, with η_i being a Gaussian white noise of zero mean and variance $\langle \eta_i(t)\eta_j(t')\rangle = 2D_r\delta(t-t')\delta_{ij}$. Here, D_r is the rotational diffusion coefficient resulting in persistence time $\tau_p = 1/D_r$. When $\tau_p \to 0$, equilibrium Brownian motion is recovered. In this work, we investigate the relaxation as the shape index p_0 and the persistence time τ_p are varied.

We carry out simulations in a square box under periodic boundary conditions [55]. The number density is set to 1. Voronoi tessellations are computed using the Boost C++ Voronoi library [56]. To obtain reliable results and improve statistical accuracy, we average the results over five independent runs for each state point. The number of cells N ranges from 256 to 10^4, and $N = 3600$ for most of our results, if not otherwise specified. We discuss below the important effect of system size on the relaxation dynamics of the active cells.

III. RESULTS AND DISCUSSION

A. Glass transition and system size dependence

A rigidity transition was identified at zero temperature by decreasing the target shape index p_0 to $p_0 \simeq 3.81$ [49,54]. In active cells, the glass transition occurs as p_0 decreases, with the transition point contingent on the values of the persistence time τ_p [3]. We first characterize the τ_p-dependent liquid-glass transition boundary by investigating the relaxation dynamics. This analysis considers the previously unexplored system size effect, and we further delve into its origin. We study the mean square displacement (MSD) $\langle \Delta r^2(t)\rangle = \langle \frac{1}{N}\sum_{i=1}^{N} \Delta\mathbf{r}_i(t)^2\rangle$, where $\Delta\mathbf{r}_i(t)$ represents the displacement of cell i during time t, and the self-intermediate scattering function (ISF) $F_s(q,t) = \langle \frac{1}{N}\sum_{j=1}^{N} e^{i\mathbf{q}\cdot\Delta\mathbf{r}_j(t)}\rangle$, with $q = |\mathbf{q}|$ being the wave number of the first peak of the static structure factor. The MSD exhibits ballistic behavior at short times, $\langle \Delta r^2(t)\rangle \sim v^2 t^2$, with $v^2 = \langle \mathbf{v}_i^2\rangle$ being the mean square velocity. We observe a convergence of MSD in the ballistic regime at $\tau_p = 0.1$, while v^2 decreases as p_0 is reduced at $\tau_p = 100$, suggesting a significant impact of activity on the velocities, as discussed in detail in Fig. 8 in Appendix B. This observation is analogous to that in the dense assembly of persistence particles [27]. At longer times, the system directly enters the diffusive regime at large p_0 in the liquid states. Conversely, we find caging, characterized by the long plateau in the MSD [Figs. 1(a) and 1(b)], and the emerging shoulder in the ISF [Figs. 1(c) and 1(d)] for a small system size before the system becomes diffusive at small p_0 in the supercooled states.

The dynamics depend significantly on system size, particularly in the supercooled regime, as observed in the ISF for $\tau_p = 0.1$ [Fig. 1(c)], as well as in both the MSD and the ISF for $\tau_p = 100$ [Figs. 1(b) and 1(d)]. One contribution to this system size dependence is long-wavelength fluctuations, which are known to be relevant in two dimensions [43–46,57], evidenced by the linear dependence of the square root of the Debye-Waller factor $\sqrt{\langle u^2\rangle}$ on $\sqrt{N}$ [Fig. 1(b), inset]. Filtering out the impact of long-wavelength fluctuations is achieved through CR measures [43–46], wherein the standard displacement $\Delta\mathbf{r}_i(t)$ in dynamical quantities is replaced by the CR displacement $\Delta\mathbf{r}_i^{\mathrm{CR}}(t) = \Delta\mathbf{r}_i(t) - 1/N_i \sum_{j=1}^{N_i} \Delta\mathbf{r}_j(t)$, with the sum extending over the N_i neighbors that particle i has at time 0. A data collapse of the CR-ISF $F_s^{\mathrm{CR}}(q,t)$ is observed for various system sizes at $\tau_p = 0.1$

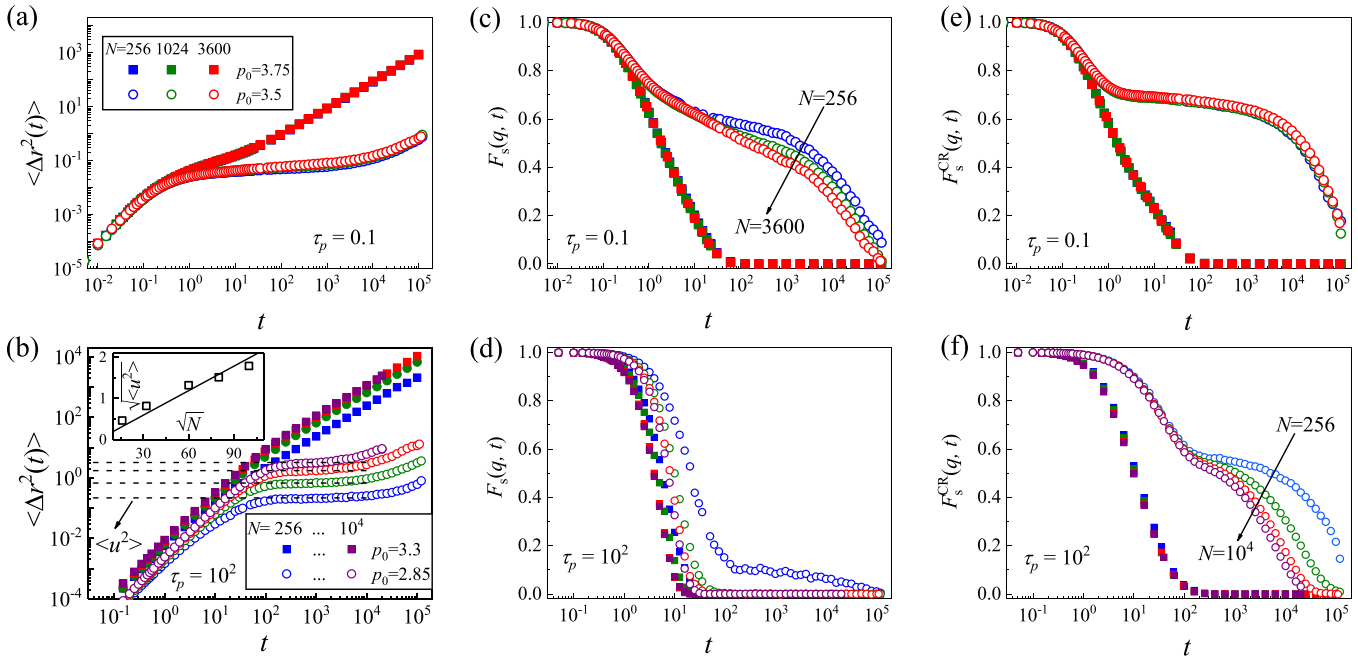

FIG. 1. Dynamics and its dependence on the system size for small and large values of persistence time. Time dependence (a) of the mean square displacement, (c) of the self-intermediate scattering function, and (e) of the cage-relative self-intermediate scattering function at persistence time $\tau_p = 0.1$. Solid squares and open circles are for $p_0 = 3.75$ and $p_0 = 3.5$, respectively. (b), (d), and (f) show the time dependence of the same quantities for $\tau_p = 10^2$ at $p_0 = 3.3$ (solid squares) and at $p_0 = 2.85$ (open circles). Different colored symbols in all main panels indicate different system sizes ranging from $N = 256$ to $N = 3600$ for $\tau_p = 0.1$ and up to 10^4 for $\tau_p = 10^2$. Black dashed lines in (b) mark the Debye-Waller factor $\langle u^2 \rangle$ evaluated from the plateau of the mean square displacement, and the inset in (b) demonstrates the linear dependence of $\langle u^2 \rangle$ on $\sqrt{N}$.

[Fig. 1(e)], where nonequilibrium effects are not prominent. At $\tau_p = 100$, conversely, data collapse is observed for the CR-ISF only in the short-time ballistic and caging regimes, not in the long-time α relaxation regime, although there is a qualitative change in the relaxation behavior from an anomalous one-step decay in the ISF [Fig. 1(d)] to a two-step decay in the CR-ISF [Fig. 1(f)]. Hence, nonequilibrium effects may also contribute to the system size dependence. This necessitates the investigation of a relatively large system at large persistence times. In Fig. 6 in Appendix A, we observe a result analogous to the CR-ISF by investigating the bond-orientational correlation function, which, by definition, is unaffected by long-wavelength fluctuations. In the following, we employ CR measures for quantities influenced by long-wavelength fluctuations and focus on a system with $N = 3600$ for all values of τ_p. This choice ensures that system size effects are negligible, even for the largest τ_p studied [$\tau_p = 100$; Fig. 1(f)].

We define the CR α relaxation time $\tau_{\rm CR}$ as $F_s^{\rm CR}(q, \tau_{\rm CR}) = e^{-1}$ and plot in Fig. 2(a) the p_0 dependence of $\tau_{\rm CR}$ for various values of τ_p. Fitting $\tau_{\rm CR}(p_0)$ with the algebraic prediction of the mode-coupling theory [58], given by $\tau_{\rm CR} \sim (p_0 - p_0^c)^\gamma$, enables the determination of the liquid-glass transition boundary p_0^c for different τ_p. p_0^c is indicated by black squares in Fig. 2(b). In Fig. 2(b), we additionally include the liquid-solid transition boundary defined by the structural order parameter, $\langle q \rangle = \langle p_i/\sqrt{a_i} \rangle = 3.81$. Our results are represented by solid violet squares, while those from Ref. [3] are shown as open black triangles. They closely coincide at small and intermediate values of persistence times but exhibit significant deviation at the largest values of τ_p we studied. This deviation may be attributed to differences in system size and the crystallization tendencies of the studied systems, as we study a polydisperse system with 3600 cells, whereas the system in Ref. [3] is monodisperse with 400 cells. Furthermore, we observe a decoupling between the dynamical glass transition and the static transition defined by $\langle q \rangle = 3.81$, which contrasts with the findings in Ref. [3] but is consistent with observations in a binary mixture of cells under thermal equilibrium [22]. We note that in Ref. [3], the dynamical transition line was determined by the disappearance of diffusivity, whereas like Sussman *et al.* [22], we define the dynamical transition based on the divergence of relaxation time. The decoupling between diffusion and relaxation is a commonly observed phenomenon [59], which could account for the disparate observations. The glass transition of active cells, illustrated in Fig. 2(b), further suggests that both deformability and persistence time impact the glass transition boundary, and p_0^c increases monotonically as τ_p decreases. However, we demonstrate in the following that the relaxation dynamics differ significantly at large and small values of τ_p.

B. Intermittent dynamics

We select nine state points with comparable $\tau_{\rm CR}$ at different values of both τ_p and p_0, as indicated in Fig. 2(a) (1–9). We first find that the persistent propulsion induces spatial correlation of the velocity, quantified by $C_v(r) = \langle \mathbf{v}(r) \cdot \mathbf{v}(0) \rangle / \langle v^2 \rangle$. In Fig. 3(a), we illustrate $C_v(r)$ for state points 5–9, where spatial correlation of the velocity is evident. The correlation extends over a larger length scale with increasing persistence

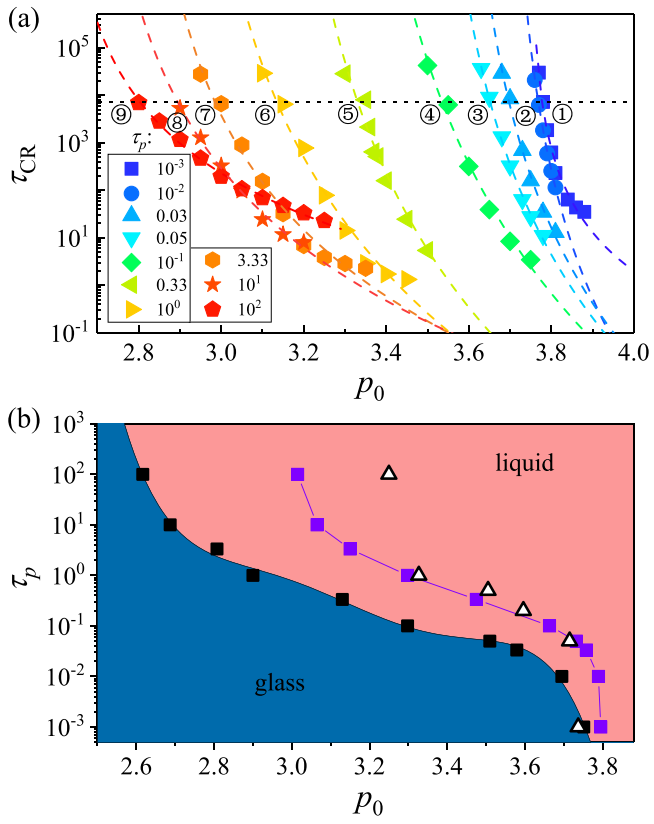

FIG. 2. The liquid-glass transition. (a) Dependence of the cage-relative α relaxation time τ_{CR} on the target shape index p_0 for various values of the persistence time τ_p. Solid lines represent the fitting results from the mode-coupling theory. We specifically select nine state points with comparable $\tau_{CR} \simeq 7100$, as indicated by the horizontal black dashed line. (b) The glass transition of active cells in the τ_p-p_0 plane. Black squares denote the mode-coupling glass transition point, while the boundary line is from a fifth-order polynomial fit. The violet squares mark the position where the structural order parameter $\langle q \rangle = \langle p_i/\sqrt{a_i} \rangle$ reaches 3.81. The open black triangles represent the fluid-solid boundary from Ref. [3] defined by $\langle q \rangle = 3.81$ for a monodisperse system with 400 cells.

time. We quantify the correlation length ξ by fitting $C_v(r)$ with the exponential form $C_v(r) \propto \exp(-r/\xi)$. In Fig. 3(b), we present the resulting τ_p dependence of ξ. Remarkably, ξ acquires finite values at $\tau_p^c \simeq 0.33$ and grows with increasing τ_p. The increasing spatial velocity correlation length has been widely observed in active systems [24–27,60], implying the necessity of a large system size to accommodate the cells and their velocity correlation. This likely serves as the origin of the observed system size effects in highly persistent cells.

In Figs. 3(c) and 3(d), we compare the time series of the average kinetic energy, $E_k(t) = \langle 0.5mv^2 \rangle$, where v represents the instantaneous velocity and the average is taken over all cells, for state points 3 and 9. These state points correspond to relatively small and large values of τ_p, respectively. We observe Gaussian-like fluctuations of $E_k(t)$ at small τ_p, resembling observations in thermally equilibrated systems. Here, relaxation events are thermally activated, exhibiting broad distributions of energy barriers in the energy landscape. In contrast, at large τ_p, $E_k(t)$ displays sudden bursts and periods of quiescence, indicating intermittent dynamics [27,30]. This behavior arises from the alternation between mechanical equilibrium states achieved through the balance between active force and interaction force and rearrangement that drives the system from one mechanical equilibrium to another.

Cell rearrangement relies on the T1 topological transition [6,23,33,41,42], illustrated in Fig. 3(g), where an edge connecting neighboring cells (in blue) disappears and a new edge connecting previously separated cells (in red) emerges. T1 transitions are tracked by checking the Voronoi neighbors of each cell throughout the simulation. The time series of the instantaneous number of T1 events $n_{T1}(t)$ is presented in Figs. 3(e) and 3(f) for state points 3 and 9. This count is obtained by comparing configurations at time t and the previous time step. A close correspondence between $E_k(t)$ and $n_{T1}(t)$ is observed. At small persistence times, $n_{T1}(t)$ deviates from zero at random times, resembling white noise. Conversely, at large persistence times, it spikes when $E_k(t)$ surges and remains at zero during periods of quiescence in $E_k(t)$. This close correlation is further visualized in Fig. 3(g), where we illustrate the local configuration at time t_2, precisely at the peak of the kinetic energy, along with the configurations at t_1 and t_3 before and after the surge. These three time points are marked at the bottom of Fig. 3(f). A T1 transition at t_2 is identified, highlighting cells (in red and blue) that participate in this T1 transition in these configurations. The T1 rearrangement is associated with large instantaneous velocities of the involved cells, as indicated by the black vectors. Facing pair cells exhibit velocities pointing in opposite directions and display fourfold features.

C. Link between relaxation and T1 transitions

Notably, as seen in Figs. 3(e) and 3(f), T1 transitions occur more frequently at small persistence times than at large ones. We therefore consistently find a higher cumulative count of T1 transitions per cell N_{T1}/N at lower persistence times, as demonstrated in Fig. 4(a). The linear dependence of N_{T1}/N on time allows us to define the T1 transition rate per cell Γ_{T1}, which decreases monotonically as the persistence time increases, as shown by the red circles in Fig. 4(c). This finding is consistent with previous results [60]. However, it is important to note that the CR α relaxation times for these state points are comparable, as indicated in Fig. 2(a). This suggests that the rate of T1 transition may not be the key parameter governing the slow α relaxation. We then turn to counting irreversible T1 transitions, where a second consecutive T1 transition does not reverse the first one, as reverse T1 transitions recover the local configuration and do not contribute to the relaxation. The time evolution of the cumulative number of irreversible T1 transitions per cell N_{T1}^{irr}/N is presented in Fig. 4(b), and the rate of irreversible T1 transitions Γ_{T1}^{irr} (red triangles) is illustrated in Fig. 4(c) for those nine selected state points with comparable τ_{CR} [Fig. 2(a)]. We first observe that Γ_{T1}^{irr} differs from Γ_{T1} by more than an order of magnitude at small τ_p. However, this difference diminishes as τ_p increases, indicating that T1 transitions are more likely to be irreversible at large τ_p. This phenomenon can be understood by examining the probability P_{irr} that two consecutive T1 transitions of the same cell are not the reverse of each other. Figure 5 illustrates P_{irr}

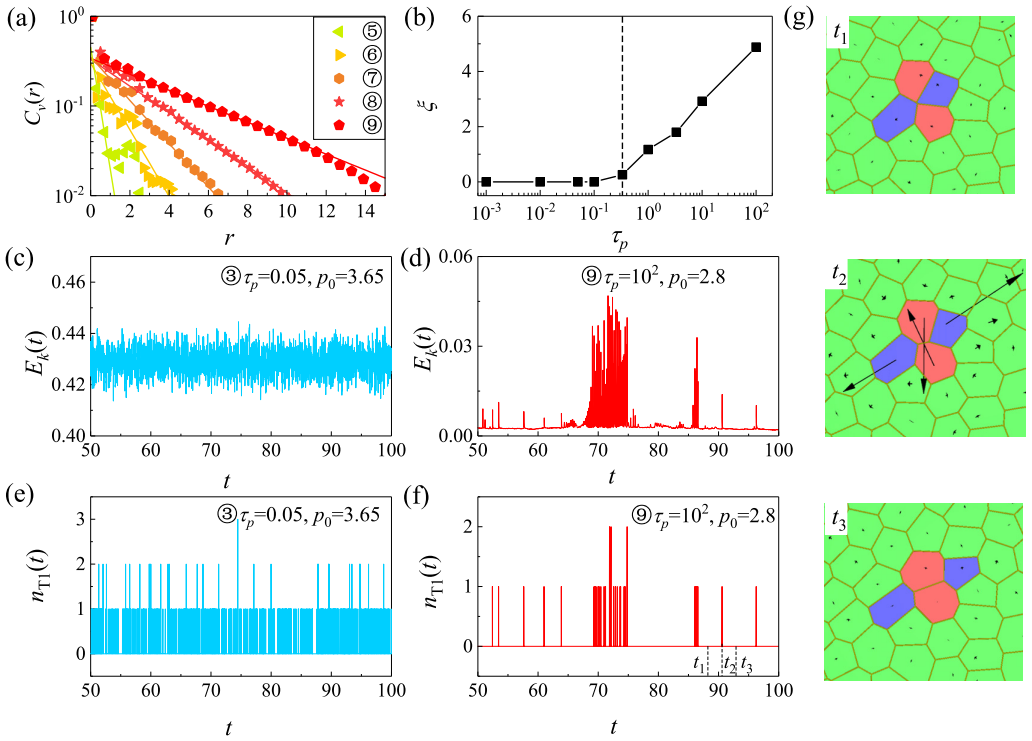

FIG. 3. Emergence of intermittent dynamics and spatial velocity correlation for a long persistence time. (a) The spatial velocity correlation function $c_v(r)$ for state points 5–9. (b) The velocity correlation length ξ as a function of the persistence time τ_p for the nine selected state points, as indicated in Fig. 2(a). The critical value τ_p^c, at which ξ diverges from zero, is denoted by the vertical dashed line in (b). Time series of (c) and (d) the kinetic energy and (e) and (f) the instantaneous number of T1 transitions for state points 3 and 9. (g) Visualization of local configurations before, during, and after the T1 transition at times t_1, t_2, and t_3, as indicated at the bottom of (f), for state point 9. Cells involved in the T1 transition are highlighted in blue and red, while others are shown in green. Velocity vectors are represented by black arrows in (g).

as a function of the time t separating the two consecutive T1 transitions for three selected values of persistence times. Regardless of τ_p, $P_{\rm irr}$ reaches a long-time plateau of 1 as the system relaxes at $\tau_{\rm CR}$, indicated by the black arrow in Fig. 5. At small τ_p, $P_{\rm irr}$ increases almost monotonically to its final value of 1. However, we observe a period of high $P_{\rm irr} \simeq 1$ at intermediate timescales within the curve, where $P_{\rm irr}$ initially rises to approximately 1, then drops to a lower value, and finally increases again as the system relaxes. The duration of this intermediate plateau is closely related to the persistence time and increases as τ_p grows. These observations suggest that persistence induces irreversible T1 transitions, with the rates of T1 transitions and irreversible T1 transitions being similar at high persistence time, in contrast to the low persistence case.

More intriguingly, $\Gamma_{\rm T1}^{\rm irr}$ reaches a plateau for small persistence times, $\tau_p \leqslant \tau_p^c \simeq 0.33$. This critical value τ_p^c coincides with the emergence of spatial velocity correlation [Fig. 3(b)] and with the onset of intermittence in the kinetic energy, quantified by the kurtosis, denoted as $\kappa = \langle [E_k(t)]^4 \rangle / \langle [E_k(t)]^2 \rangle^2$, where the angular brackets represent the average over different times. The kurtosis κ is presented as black squares in Fig. 4(c), with black dashed lines marking the critical value of τ_p^c, at which κ begins to exceed 3, the kurtosis value corresponding to Gaussian fluctuations.

At large persistence times, $\tau_p > \tau_p^c$, a distinct behavior is observed where $\Gamma_{\rm T1}^{\rm irr}$ decreases with increasing τ_p, indicating different relaxation modes when dynamics become intermittent in persistent cells. Within these cells, mechanical equilibrium is readily achieved with $\mathbf{f}_i^m + \mathbf{f}_i^a = -\nabla_i e + v_0 \hat{n}_i = 0$ [27,30], leading to prolonged trapping of the system in the energy minimum of an effective potential $e^{\rm eff} = e - \Sigma_i v_0 \hat{n}_i \cdot \vec{r}_i$. The breaking of this mechanical equilibrium relies on the change in $\hat{n}_i$ with a typical timescale of τ_p as the system slowly evolves its position. An increase in τ_p consequently results in a decrease of rearranging events and, as a consequence, a decrease in the irreversible T1 transition rate $\Gamma_{\rm T1}^{\rm irr}$. As T1 transitions become rare, the mean velocity magnitude $v = \langle |\mathbf{v}_i| \rangle$ also decreases with increasing τ_p at $\tau_p > \tau_p^c$ (Fig. 8 in Appendix B). This contrasts with the observation that v reaches a plateau value close to $v_0 = 1.0$ at small values of τ_p (Fig. 8 in Appendix B). The decrease in both the irreversible T1 transition rate and the mean velocity magnitude contributes to the slow relaxation of the system. This suggests that additional relaxation modes may compensate for this decrease, considering that the final CR α relaxation time is comparable to that at low persistence times.

At high τ_p, the spatial velocity correlation leads to the collective motion of cells with a typical length scale ξ. The mechanical equilibrium condition further leads cells to move with a constant velocity, resulting in a long ballistic and superdiffusive region before caging. This introduces a mode in which cells relax collectively. Consequently, in Fig. 7 in Appendix B, we observe that as τ_p increases, the superdiffu-

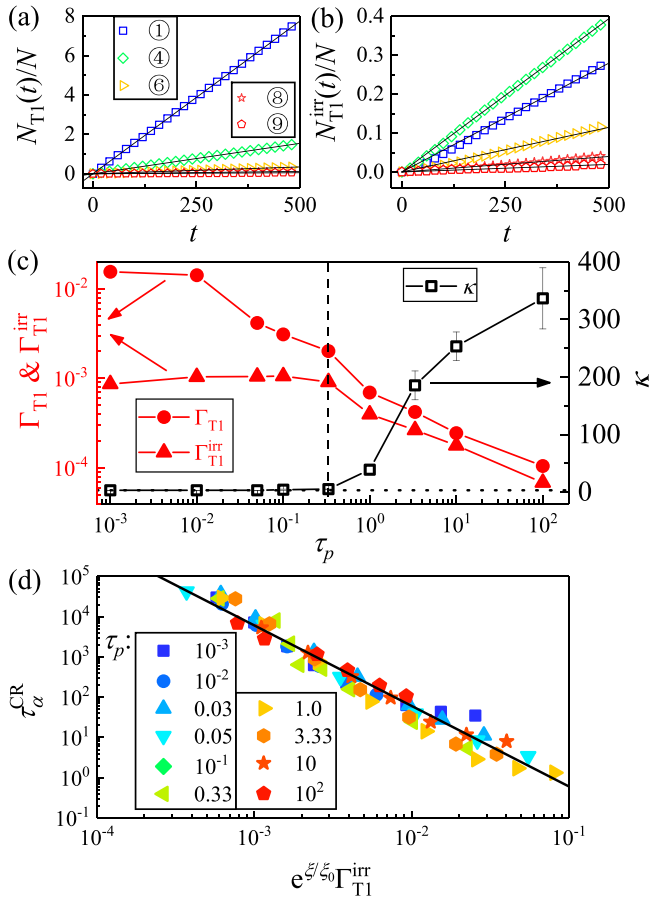

FIG. 4. Link between structural relaxation and T1 transitions. Time dependence of the cumulative count of (a) all T1 transitions per cell, denoted as N_{T1}/N, and (b) irreversible T1 transitions per cell, denoted as N_{T1}^{irr}/N. (c) The kurtosis of the kinetic energy κ (black squares) and the rate of all (Γ_{T1}) and irreversible (Γ_{T1}^{irr}) T1 transitions as a function of the persistence time τ_p. (d) The relaxation time τ_{CR} as a function of $\exp(\xi/\xi_0)\Gamma_{T1}^{irr}$ at different persistence times, as detailed in the legend.

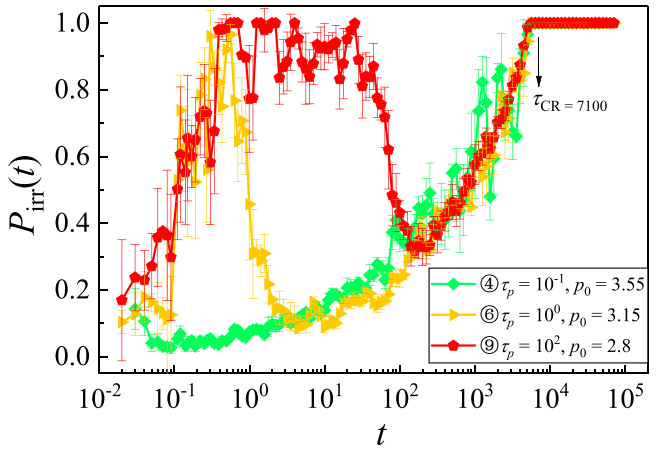

FIG. 5. Time dependence of the probability of irreversible consecutive T1 transitions for different values of p_0 at persistence times $\tau_p = 0.1$ (green diamonds), $\tau_p = 1$ (yellow triangles), and $\tau_p = 10^2$ (red pentagons). The error bars represent the standard deviation calculated from five independent runs.

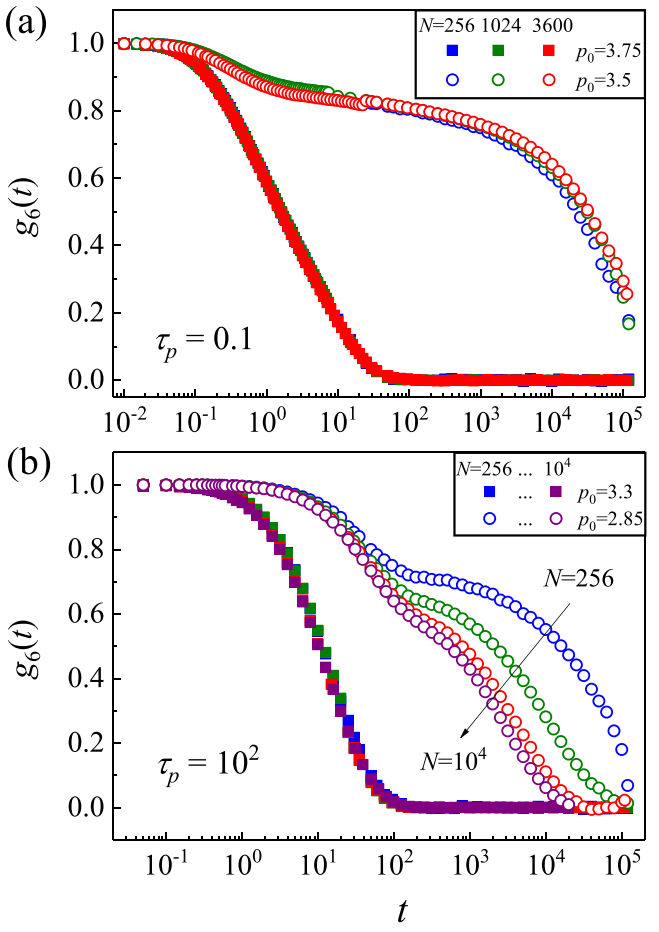

FIG. 6. Bond-orientational correlation functions at small and large values of persistence time. Time dependence of the bond-orientational correlation functions $g_6(t)$ for (a) $\tau_p = 0.1$ and (b) $\tau_p = 100$. Solid squares and open circles represent different values of p_0, while different colored symbols correspond to different system sizes, as detailed in the legend.

sive region extends to a larger timescale, and the subsequent caging plateau starts at later times. This leads to the gradual shrinking of the caging regime as τ_p increases for $\tau_p > \tau_p^c$, whereas this phenomenon is absent at small τ_p (Fig. 7 in Appendix B).

Taking into account collective relaxation, we plot the CR α relaxation time in Fig. 4(d) as a function of $\exp(\xi/\xi_0)\Gamma_{T1}^{irr}$, where ξ_0 is a constant ranging from approximately 0.7 to 2.1 as τ_p varies from 1.0 to 10^2. The data collapse well to a universal function,

$$\tau_{CR} \propto \left[\exp(\xi/\xi_0)\Gamma_{T1}^{irr}\right]^{-\alpha}, \tag{2}$$

with the dynamical critical exponent $\alpha \simeq 1.9$. This collapse spans approximately 5 orders of magnitude of the CR α relaxation time and a large range of τ_p.

The above results demonstrate clear relaxation pictures unified within the function [Eq. (2)] in active cells. Specifically, at small persistence times, $\tau_p \leqslant \tau_p^c$, the spatial velocity correlation is absent, and thus, $\xi = 0$. In these cases, the α relaxation process is solely determined by the irreversible T1 transition rates. In these nearly equilibrated cells, the

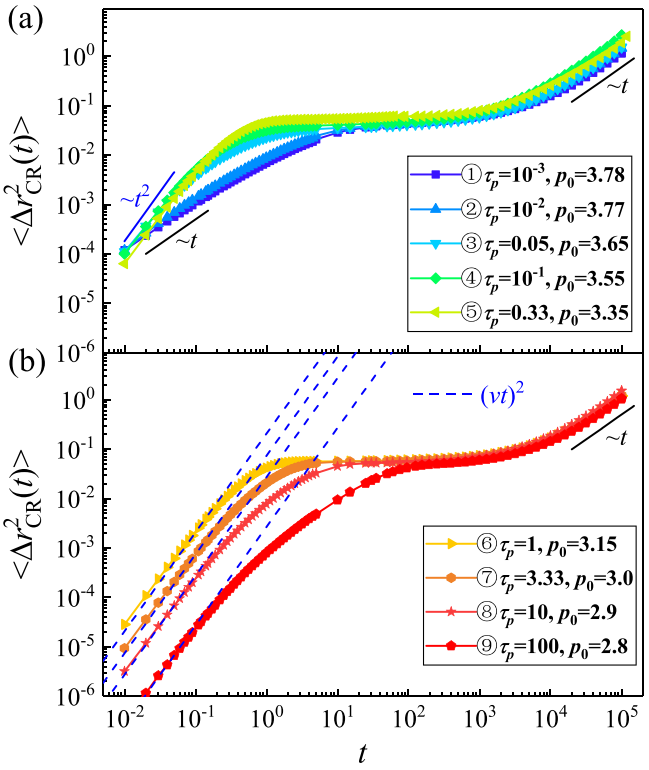

FIG. 7. Different short time dynamics among state points with similar relaxation times for different values of persistence time. The time evolution of the cage-relative mean square displacements for the nine selected state points indicated in Fig. 2(a) in the main text. (a) illustrates results for $\tau_p \leqslant \tau_p^c = 0.33$, and (b) corresponds to $\tau_p > \tau_p^c$. Brownian behavior is represented by the black lines, while the blue lines denote ballistic behavior.

relaxation process is dominated by the rate of jumps between energy barriers within the energy landscape. These jumps are facilitated by irreversible T1 transitions, and thus, their rates $\Gamma_{\mathrm{T1}}^{\mathrm{irr}}$ play a pivotal role in the relaxation dynamics. In contrast, in more persistent cells, irreversible T1 transitions become more infrequent. Cells may shift with a constant velocity collectively with a typical length scale ξ as the mechanical equilibrium condition at short times is attained. This collective persistent motion also contributes to the relaxation dynamics, introducing a dependence of the relaxation time on the additional parameter ξ. These distinct relaxation processes are well described by the universal power-law function, reminiscent of the power-law form of the mode-coupling theory. The divergence of the CR α relaxation time occurs at the mode-coupling transition point, where the irreversible T1 transition rates reach zero. Persistent motion induces spatial velocity correlation and triggers collective relaxation, leading to a flatter divergence of τ_{CR} as irreversible T1 transition nearly vanishes.

IV. CONCLUSIONS

In summary, we investigated the liquid-glass transition in confluent monolayers of active epithelial cells using the self-propelled Voronoi model. The glass transition is triggered by decreasing the deformability p_0 and/or the persistence time τ_p, enabling us to identify the glass transition line in the τ_p vs p_0 plane. We demonstrated the influence of system size on dynamics, arising from long-wavelength fluctuations at small persistence times in nearly equilibrated cells and, additionally, from nonequilibrium effects at large persistence times in active cells. We applied CR measures for dynamical quantities influenced by long-wavelength fluctuations and conducted studies of relatively large systems to ensure negligible finite size effects. While supercooled dynamics occur at both small and large persistence times, self-propulsions qualitatively alter how the system relaxes and explores its energy landscape. Specifically, we identified spatial velocity correlations and intermittent dynamics associated with intermittent T1 transitions, inducing a distinct relaxation mode in highly persistent cells compared to nearly equilibrated cells. However, these different relaxation modes are described by a universal power-law dependence of CR α relaxation time on the exponential of the velocity correlation length times the irreversible T1 transition rate. Our results may inspire novel glass transition theories and stimulate numerical and experimental research into the relaxation dynamics of supercooled active systems. For instance, future studies could investigate the dependence of relaxation, intermittent dynamics, and both reversible and irreversible T1 rates on the T1 stalling time [6].

ACKNOWLEDGMENT

This work is supported by the National Natural Science Foundation of China (Grants No. 12374204 and No. 12105012).

APPENDIX A: BOND-ORIENTATIONAL CORRELATION FUNCTIONS

In Figs. 1(e) and 1(f), we presented cage-relative intermediate scattering functions (CR-ISFs) varying p_0 for different values of τ_p. In this context, we explore an additional quantity, the bond-orientational correlation function $g_6(t)$, which, by definition, is unaffected by long-wavelength fluctuations. $g_6(t)$ is defined as $g_6(t) = \langle \sum_n \Psi_6^n(t)[\Psi_6^n(0)]^* \rangle / \langle \sum_n |\Psi_6^n(0)|^2 \rangle$. Here, $\Psi_6^n(t) = \sum_m (N_b^n)^{-1} e^{i6\theta_n^m(t)}$, where N_b^n is the number of Voronoi nearest neighbors of cell n, $\theta_n^m(t)$ is the angle between cell n and cell m at time t, and $*$ denotes the complex conjugate. In Fig. 6, we present the time dependence of $g_6(t)$ for the same state points presented in Fig. 1 in the main text. We find a data collapse of $g_6(t)$ for different system sizes at both small and large values of p_0 for $\tau_p = 0.1$ [Fig. 6(a)], suggesting that the effects of the system size on $g_6(t)$ are negligible. Differently, at $\tau_p = 100$ [Fig. 7(b)], the data collapse is evident only at large values of p_0 when the dynamics are fast. We observe a clear system size dependence for $p_0 = 2.85$, and this requires the study of the system at a relatively large system size ($N \geqslant 3600$). This observation parallels the behavior observed in $F_s^{\mathrm{CR}}(q,t)$, suggesting that CR quantities effectively filter out the impact of long-wavelength fluctuations on the dynamics.

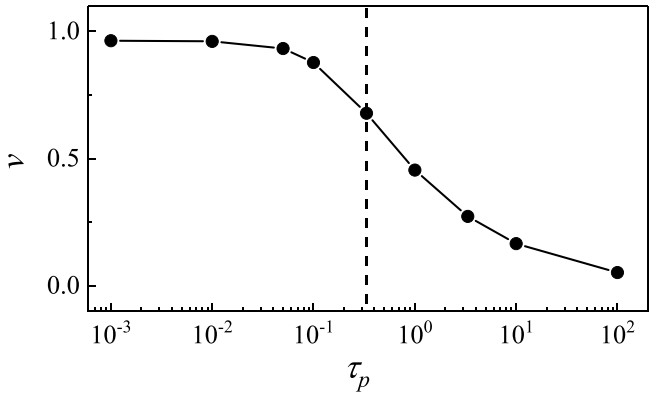

FIG. 8. The mean magnitude of velocity drops with increasing persistence time. The mean magnitude of the velocity as a function of the persistence time τ_p for the nine selected state points marked in Fig. 2(a) in the main text. The vertical dashed line marks the critical value of τ_p, $\tau_p^c = 0.33$, beyond which intermittent dynamics occur.

APPENDIX B: τ_p DEPENDENCE OF THE SUPERCOOLED DYNAMICS

In Fig. 2(a), we selected nine state points with comparable cage-relative α relaxation times at different values of p_0 for various persistence times τ_p. Here, we illustrate their cage-relative mean square displacements (CR-MSDs) in Figs. 7(a) and 7(b), respectively, for τ_p values below (or at) and above $\tau_p^c \simeq 0.33$. At very small values of τ_p ($\tau_p = 10^{-3}$ and 10^{-2}), the CR-MSD [Fig. 7(a)] exhibits diffusive behavior at short times, suggesting that the system recovers Brownian dynamics when τ_p is sufficiently small. This short-time Brownian behavior transitions to ballistic dynamics for larger τ_p. However, the CR-MSD converges in the ballistic region, indicating that v^2 remains constant across different τ_p. In Fig. 8, we directly plot the mean velocity magnitude $v = \langle |\mathbf{v}_i| \rangle$ at different values of τ_p for these nine state points and consistently observe that v reaches plateau values close to the active velocity $v_0 = 1.0$ at small persistence. In contrast, at large τ_p, v systematically drops (Fig. 8) with increasing τ_p, leading to the nonconvergence of CR-MSD in the ballistic region [Fig. 7(b)]. Despite these different short-time dynamics, the subsequent caging regime is evident, characterized by a plateau region in the CR-MSD.

Intriguingly, the initiation time and duration of the caging regime are influenced by self-propulsion. Specifically, for small values of τ_p ($\tau_p \leqslant \tau_p^c$), there is no spatially correlated motion, and cells move randomly before sufficiently interacting and being constrained by neighboring cells. The shift from Brownian to ballistic short-time dynamics at around $\tau_p = 10^{-2}$ causes an earlier onset of caging due to the faster ballistic motion compared to Brownian motion. Beyond τ_p^c, the dynamics qualitatively differ as self-propulsion induces strong spatially correlated motion. The initiation time of the caging regime is systematically delayed with the contraction of the caging regime as τ_p increases. Before entering the caging regime, the system remains superdiffusive for an extended period, with cells undergoing directed and spatially correlated motion. Although v significantly drops as τ_p increases (Fig. 8), spatially correlated motion introduces a relaxation mode that compensates for the sluggish dynamics, bringing the α relaxation time comparable to that of systems with small persistence times that have larger values of v. This suggests a correlation between the α relaxation time and spatially correlated motion, as depicted in Fig. 4(d) in the main text.

[1] M. C. Marchetti, J. F. Joanny, S. Ramaswamy, T. B. Liverpool, J. Prost, M. Rao, and R. A. Simha, Hydrodynamics of soft active matter, Rev. Mod. Phys. **85**, 1143 (2013).
[2] C. Bechinger, R. Di Leonardo, H. Löwen, C. Reichhardt, G. Volpe, and G. Volpe, Active particles in complex and crowded environments, Rev. Mod. Phys. **88**, 045006 (2016).
[3] D. Bi, X. Yang, M. C. Marchetti, and M. L. Manning, Motility-driven glass and jamming transitions in biological tissues, Phys. Rev. X **6**, 021011 (2016).
[4] A. Pasupalak, Li Yan-Wei, R. Ni, and M. Pica Ciamarra, Hexatic phase in a model of active biological tissues, Soft Matter **16**, 3914 (2020).
[5] B. Loewe, M. Chiang, D. Marenduzzo, and M. C. Marchetti, Solid-liquid transition of deformable and overlapping active particles, Phys. Rev. Lett. **125**, 038003 (2020).
[6] A. Das, S. Sastry, and D. Bi, Controlled neighbor exchanges drive glassy behavior, intermittency, and cell streaming in epithelial tissues, Phys. Rev. X **11**, 041037 (2021).
[7] J. H. Kim, X. Serra-Picamal, D. T. Tambe, E. H. Zhou, C. Y. Park, M. Sadati, J.-A. Park, R. Krishnan, B. Gweon, E. Millet, J. P. Butler, X. Trepat, and J. J. Fredberg, Propulsion and navigation within the advancing monolayer sheet, Nat. Mater. **12**, 856 (2013).
[8] S. Garcia, E. Hannezo, J. Elgeti, J.-F. Joanny, P. Silberzan, and N. S. Gov, Physics of active jamming during collective cellular motion in a monolayer, Proc. Natl. Acad. Sci. USA **112**, 15314 (2015).
[9] J.-M. Armengol-Collado, L. N. Carenza, J. Eckert, D. Krommydas, and L. Giomi, Epithelia are multiscale active liquid crystals, Nat. Phys. **19**, 1773 (2023).
[10] D. L. Barton, S. Henkes, C. J. Weijer, and R. Sknepnek, Active vertex model for cell-resolution description of epithelial tissue mechanics, PLoS Comput. Biol. **13**, e1005569 (2017).
[11] M. Basan, J. Elgeti, E. Hannezo, W.-J. Rappel, and H. Levine, Alignment of cellular motility forces with tissue flow as a mechanism for efficient wound healing, Proc. Natl. Acad. Sci. USA **110**, 2452 (2013).
[12] M. Poujade, E. Grasland-Mongrain, A. Hertzog, J. Jouanneau, P. Chavrier, B. Ladoux, A. Buguin, and P. Silberzan, Collective migration of an epithelial monolayer in response to a model wound, Proc. Natl. Acad. Sci. USA **104**, 15988 (2007).
[13] C. Manli, H. David, and J. W. Cornelis, Collective epithelial and mesenchymal cell migration during gastrulation, Curr. Genomics **13**, 267 (2012).
[14] E.-M. Schötz, M. Lanio, J. A. Talbot, and M. L. Manning, Glassy dynamics in three-dimensional

embryonic tissues, J. R. Soc. Interface **10**, 20130726 (2013).
[15] T. E. Angelini, E. Hannezo, X. Trepat, M. Marquez, J. J. Fredberg, and D. A. Weitz, Glass-like dynamics of collective cell migration, Proc. Natl. Acad. Sci. USA **108**, 4714 (2011).
[16] N. V. Jordan, G. L. Johnson, and A. N. Abell, Tracking the intermediate stages of epithelial-mesenchymal transition in epithelial stem cells and cancer, Cell Cycle **10**, 2865 (2011).
[17] H. Tanaka and S. Ogishima, Network biology approach to epithelial–mesenchymal transition in cancer metastasis: Three stage theory, J. Mol. Cell Biol. **7**, 253 (2015).
[18] R. Kalluri and R. A. Weinberg, The basics of epithelial-mesenchymal transition, J. Clin. Invest. **119**, 1420 (2009).
[19] J.-A. Park *et al.*, Unjamming and cell shape in the asthmatic airway epithelium, Nat. Mater. **14**, 1040 (2015).
[20] A. Puliafito, L. Hufnagel, P. Neveu, S. Streichan, A. Sigal, D. K. Fygenson, and B. I. Shraiman, Collective and single cell behavior in epithelial contact inhibition, Proc. Natl. Acad. Sci. USA **109**, 739 (2012).
[21] T. E. Angelini, E. Hannezo, X. Trepat, J. J. Fredberg, and D. A. Weitz, Cell migration driven by cooperative substrate deformation patterns, Phys. Rev. Lett. **104**, 168104 (2010).
[22] D. M. Sussman, M. Paoluzzi, M. C. Marchetti, and M. L. Manning, Anomalous glassy dynamics in simple models of dense biological tissue, Europhys. Lett. **121**, 36001 (2018).
[23] Y.-W. Li, L. L. Y. Wei, M. Paoluzzi, and M. P. Ciamarra, Softness, anomalous dynamics, and fractal-like energy landscape in model cell tissues, Phys. Rev. E **103**, 022607 (2021).
[24] L. Caprini, U. M. B. Marconi, and A. Puglisi, Spontaneous velocity alignment in motility-induced phase separation, Phys. Rev. Lett. **124**, 078001 (2020).
[25] L. Caprini, U. M. B. Marconi, C. Maggi, M. Paoluzzi, and A. Puglisi, Hidden velocity ordering in dense suspensions of self-propelled disks, Phys. Rev. Res. **2**, 023321 (2020).
[26] S. Henkes, K. Kostanjevec, J. M. Collinson, R. Sknepnek, and E. Bertin, Dense active matter model of motion patterns in confluent cell monolayers, Nat. Commun. **11**, 1405 (2020).
[27] Y.-E. Keta, R. L. Jack, and L. Berthier, Disordered collective motion in dense assemblies of persistent particles, Phys. Rev. Lett. **129**, 048002 (2022).
[28] Y. Katz, K. Tunstrøm, C. C. Ioannou, C. Huepe, and I. D. Couzin, Inferring the structure and dynamics of interactions in schooling fish, Proc. Natl. Acad. Sci. USA **108**, 18720 (2011).
[29] J. Dunkel, S. Heidenreich, K. Drescher, H. H. Wensink, M. Bär, and R. E. Goldstein, Fluid dynamics of bacterial turbulence, Phys. Rev. Lett. **110**, 228102 (2013).
[30] R. Mandal, P. J. Bhuyan, P. Chaudhuri, C. Dasgupta, and M. Rao, Extreme active matter at high densities, Nat. Commun. **11**, 2581 (2020).
[31] Y.-E. Keta, R. Mandal, P. Sollich, R. L. Jack, and L. Berthier, Intermittent relaxation and avalanches in extremely persistent active matter, Soft Matter **19**, 3871 (2023).
[32] G. Szamel and E. Flenner, Extremely persistent dense active fluids, Soft Matter **20**, 5237 (2024).
[33] D. B. Staple, R. Farhadifar, J.-C. Röper, B. Aigouy, S. Eaton, and F. Jülicher, Mechanics and remodelling of cell packings in epithelia, Eur. Phys. J. E **33**, 117 (2010).
[34] N. L. Christos, H. Norman, J. Arben, and L. Hartmut, Interactions and phase behaviour of polyelectrolyte star solutions, J. Phys.: Condens. Matter **15**, S233 (2003).
[35] M. Watzlawek, C. N. Likos, and H. Löwen, Phase diagram of star polymer solutions, Phys. Rev. Lett. **82**, 5289 (1999).
[36] C. von Ferber, A. Jusufi, C. N. Likos, H. Löwen, and M. Watzlawek, Triplet interactions in star polymer solutions, Eur. Phys. J. E **2**, 311 (2000).
[37] T. Terao, Counterion distribution and many-body interaction in charged dendrimer solutions, Mol. Phys. **104**, 2507 (2006).
[38] A. R. Denton, Counterion penetration and effective electrostatic interactions in solutions of polyelectrolyte stars and microgels, Phys. Rev. E **67**, 011804 (2003).
[39] N. Brodu, J. A. Dijksman, and R. P. Behringer, Multiple-contact discrete-element model for simulating dense granular media, Phys. Rev. E **91**, 032201 (2015).
[40] R. Hohler and S. Cohen-Addad, Many-body interactions in soft jammed materials, Soft Matter **13**, 1371 (2017).
[41] D. Weaire and N. Rivier, Soap, cells and statistics—Random patterns in two dimensions, Contemp. Phys. **25**, 59 (1984).
[42] D. Bi, J. H. Lopez, J. M. Schwarz, and M. L. Manning, Energy barriers and cell migration in densely packed tissues, Soft Matter **10**, 1885 (2014).
[43] H. Shiba, Y. Yamada, T. Kawasaki, and K. Kim, Unveiling dimensionality dependence of glassy dynamics: 2D infinite fluctuation eclipses inherent structural relaxation, Phys. Rev. Lett. **117**, 245701 (2016).
[44] S. Vivek, C. P. Kelleher, P. M. Chaikin, and E. R. Weeks, Long-wavelength fluctuations and the glass transition in two dimensions and three dimensions, Proc. Natl. Acad. Sci. USA **114**, 1850 (2017).
[45] B. Illing, S. Fritschi, H. Kaiser, C. L. Klix, G. Maret, and P. Keim, Mermin–Wagner fluctuations in 2D amorphous solids, Proc. Natl. Acad. Sci. USA **114**, 1856 (2017).
[46] Y.-W. Li, C. K. Mishra, Z.-Y. Sun, K. Zhao, T. G. Mason, R. Ganapathy, and M. Pica Ciamarra, Long-wavelength fluctuations and anomalous dynamics in 2-dimensional liquids, Proc. Natl. Acad. Sci. USA **116**, 22977 (2019).
[47] L. Galliano, M. E. Cates, and L. Berthier, Two-dimensional crystals far from equilibrium, Phys. Rev. Lett. **131**, 047101 (2023).
[48] R. Farhadifar, J.-C. Röper, B. Aigouy, S. Eaton, and F. Jülicher, The influence of cell mechanics, cell-cell interactions, and proliferation on epithelial packing, Curr. Biol. **17**, 2095 (2007).
[49] D. Bi, J. H. Lopez, J. M. Schwarz, and M. L. Manning, A density-independent rigidity transition in biological tissues, Nat. Phys. **11**, 1074 (2015).
[50] M. L. Manning, R. A. Foty, M. S. Steinberg, and E.-M. Schoetz, Coaction of intercellular adhesion and cortical tension specifies tissue surface tension, Proc. Natl. Acad. Sci. USA **107**, 12517 (2010).
[51] A. G. Fletcher, M. Osterfield, R. E. Baker, and S. Y. Shvartsman, Vertex models of epithelial morphogenesis, Biophys. J. **106**, 2291 (2014).
[52] X. Li, A. Das, and D. Bi, Mechanical heterogeneity in tissues promotes rigidity and controls cellular invasion, Phys. Rev. Lett. **123**, 058101 (2019).
[53] F. Giavazzi, M. Paoluzzi, M. Macchi, D. Bi, G. Scita, M. L. Manning, R. Cerbino, and M. C. Marchetti, Flocking transitions in confluent tissues, Soft Matter **14**, 3471 (2018).
[54] Y.-W. Li and M. P. Ciamarra, Role of cell deformability in the two-dimensional melting of biological tissues, Phys. Rev. Mater. **2**, 045602 (2018).

[55] M. Allen, *Computer Simulation of Liquids* (Oxford University Press, Oxford, 1987).

[56] B. Schling, *The Boost C++ Libraries* (XML Press, Laguna Hills, CA, 2011).

[57] N. D. Mermin and H. Wagner, Absence of ferromagnetism or antiferromagnetism in one- or two-dimensional isotropic Heisenberg models, Phys. Rev. Lett. **17**, 1133 (1966).

[58] M. D. Ediger, Spatially heterogeneous dynamics in supercooled liquids, Annu. Rev. Phys. Chem. **51**, 99 (2000).

[59] Y.-W. Li, Y.-L. Zhu, and Z.-Y. Sun, Decoupling of relaxation and diffusion in random pinning glass-forming liquids, J. Chem. Phys. **142**, 124507 (2015).

[60] J. A. Mitchel, A. Das, M. J. O'Sullivan, I. T. Stancil, S. J. DeCamp, S. Koehler, O. H. Ocaña, J. P. Butler, J. J. Fredberg, M. A. Nieto, D. Bi, and J.-A. Park, In primary airway epithelial cells, the unjamming transition is distinct from the epithelial-to-mesenchymal transition, Nat. Commun. **11**, 5053 (2020).